Measuring the Interaction of Transcription Factor Nrf2 with Its Negative Regulator Keap1 in Single Live Cells by an Improved FRET/FLIM Analysis

Dikovskaya, Dina; Appleton, Paul; Bento-Pereira, Claudia; Dinkova-Kostova, Albena

Published in:
Chemical Research in Toxicology

DOI:
10.1021/acs.chemrestox.8b00354

Publication date:
2019

Chemical Research in Toxicology

Article

Cite This: Chem. Res. Toxicol. 2019, 32, 500−512

pubs.acs.org/crt

Measuring the Interaction of Transcription Factor Nrf2 with Its Negative Regulator Keap1 in Single Live Cells by an Improved FRET/FLIM Analysis

Dina Dikovskaya,[*,†] Paul L. Appleton,[‡] Claudia Bento-Pereira,[†] and Albena T. Dinkova-Kostova[*,†,§]

[†]Jacqui Wood Cancer Centre, Division of Cellular Medicine, School of Medicine, University of Dundee, Dundee DD1 9SY, Scotland, United Kingdom

[‡]Dundee Imaging Facility, School of Life Sciences, University of Dundee, Dundee DD1 5EH, Scotland, United Kingdom

[§]Department of Pharmacology and Molecular Sciences and Department of Medicine, Johns Hopkins University School of Medicine, Baltimore, Maryland 21205, United States

Supporting Information

ABSTRACT: Transcription factor NF-E2 p45-related factor 2 (Nrf2) and its principal negative regulator, Kelch-like ECH-associated protein 1 (Keap1), comprise a molecular effector and sensor system that robustly responds to perturbations of the cellular redox homeostasis by orchestrating a comprehensive cytoprotective program. Under homeostatic conditions, Nrf2 is a short-lived protein, which is targeted for ubiquitination and proteasomal degradation. Upon encounter of electrophiles, oxidants, or pro-inflammatory stimuli, the cysteine sensors in Keap1 are chemically modified, rendering Keap1 unable to target Nrf2 for degradation, and consequently leading to accumulation of the transcription factor and enhanced transcription of cytoprotective genes. A detailed understanding of the protein−protein interactions between Nrf2 and Keap1 has been achieved by use of various in vitro systems, but few assays are available to assess these interactions in the context of the living cell. We previously developed an imaging-based FLIM/FRET methodology to visualize and measure the interaction between Nrf2 and Keap1 in single cells. Here, our goal was to improve this methodology in order to increase throughput and precision, and decrease cell-to-cell variability. To eliminate the possibility of orientation bias, we incorporated a flexible linker between Keap1 and the FRET acceptor fluorescent protein tag. To ensure the correct image capture of Nrf2 fused to the FRET donor fluorescent protein tag, we matched the maturation time of the fluorescent tag to the half-life of the endogenous Nrf2, by using sfGFP as the FRET donor. Using a global binning approach increased the assay throughput, whereas including the measured instrument response function in the analysis improved precision. The application of this methodology revealed a strong covariation of the results with the expression level of the acceptor. Taking the acceptor level into account circumvented cell-to-cell variability and enhanced sensitivity of the measurements of the Keap1−Nrf2 interaction in live cells.

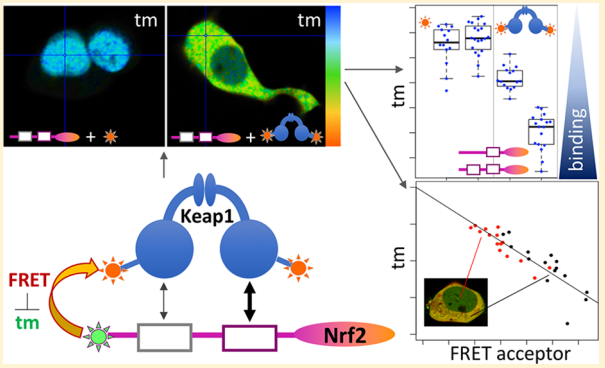

INTRODUCTION

Transcription factor NF-E2 p45-related factor 2 (Nrf2, gene name *NFE2L2*) regulates the expression of a large network of genes encoding inducible cytoprotective proteins that allow mammalian cells and organisms to adapt and survive under various conditions of stress.[1] Together with its principal negative regulator, Kelch-like ECH-associated protein 1 (Keap1), Nrf2 forms a molecular effector and sensor system that robustly responds to perturbations of the cellular redox balance and orchestrates a comprehensive defense program, which in turn restores homeostasis.[2] The Nrf2 status affects the production of reactive oxygen species (ROS) by the two major ROS-producing systems, mitochondria and NADPH oxidase.[3] Among the Nrf2 transcriptional targets are proteins with critical roles in the generation and utilization of reducing equivalents such as NADPH and reduced glutathione (GSH), as well as thioredoxin, thioredoxin reductase, peroxiredoxin, and sulfiredoxin, which collectively provide compartmentalized redox sensing of ROS to maintain redox balance under homeostatic conditions.[4−6] By regulating NAD(P)H:quinone oxidoreductase 1 (NQO1), Nrf2 prevents quinones (which are generated during metabolism of endogenous compounds, such as estrogens and dopamine, as well as from dietary and environmental sources) from participating in redox cycling reactions and glutathione depletion.[7] By regulating heme oxygenase 1

Special Issue: Redox Pathways in Chemical Toxicology

Received: November 16, 2018
Published: February 22, 2019

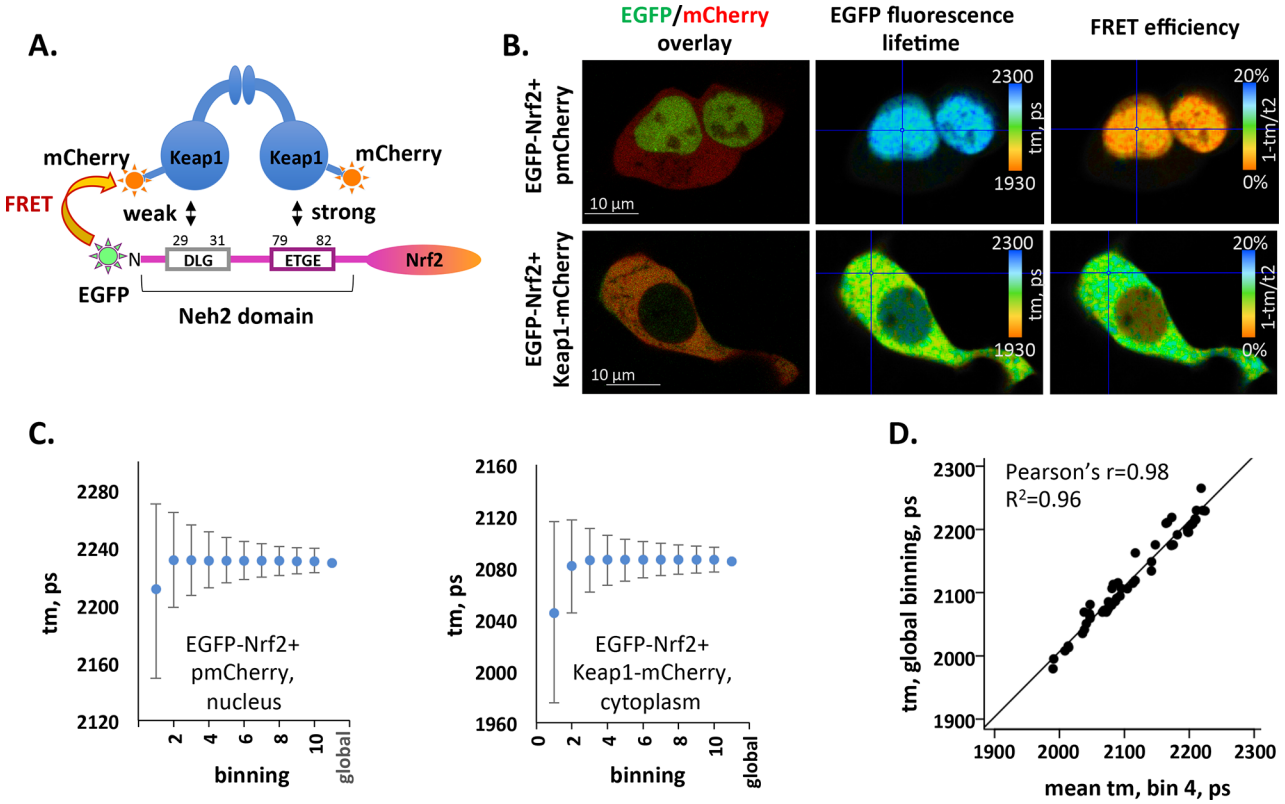

Figure 1. Measuring the Nrf2−Keap1 interaction with FLIM-FRET. (A) An interaction between Nrf2 N-terminally tagged with EGFP and Keap1 C-terminally tagged with mCherry elicits FRET. EGFP is directly adjacent to the Neh2 domain of Nrf2 that contains two unequal binding sites for Keap1—the low affinity DLG motif and the high affinity ETGE motif (rectangles), at the indicated positions. Each of the sites interacts with the C-terminal Kelch domain (blue circle) of dimeric Keap1, which positions mCherry next to EGFP and mediates FRET. Please note that Nrf2 and Keap1 are not drawn to scale. (B) Live HEK293 cells cotransfected with EGFP−Nrf2 and either free mCherry (top) or Keap1−mCherry (bottom) were first imaged to detect EGFP (green in overlay) and mCherry (red in overlay) fluorescence (left panels). The fluorescence lifetime (tm) of EGFP was determined in the same cells by one-exponential decay fitting of the photon arriving times, measured in each pixel using FLIM (middle panels, spectrally color-coded between 1930 and 2300 as indicated). FRET efficiency calculated as in formula D from the same data (right panels) is spectrally color-coded between 0 and 20%. To determine FRET efficiency, the fluorescence lifetime of EGFP in the absence of acceptor (t2) was fixed at 2275 ps, and the fluorescence lifetime in the presence of acceptor (tm) calculated from fitting the two-exponential decay model as in formula C. (C) The mean (dots) and standard deviation (error bars) of fluorescence lifetime within the same nuclear area (left, top cell in B) or the same cytoplasmic area (right, bottom cell in B) determined by fitting a one-exponential decay model to the data with increasing level of binning. Global binning combines the entire nucleus (left) or the entire cytoplasm (right) into one data set and thus produces a single tm value. (D) Mean tm values determined in a region that outlines the entire nucleus or the entire cytoplasm analyzed with bin 4 correlate well with single tm values determined in the same region analyzed using global binning. One-exponential decay fitting was applied to all. Each dot corresponds to the nucleus or the cytoplasm of individual cells measured in cells transfected with EGFP−Nrf2 with or without mCherry or Keap1−mCherry (to cover the entire range of values), and the line represents a linear regression fitted to the data, with Pearson correlation coefficient (Pearson's r) and R^2 shown.

(HMOX1) and biliverdin reductase, Nrf2 contributes to the synthesis of bilirubin, the most potent nonpolar physiological antioxidant.[8]

In addition to redox, Nrf2 has a role in intermediary metabolism, including the metabolism of nucleotides,[9] amino acids,[10] and lipids,[11,12] and in providing substrates for mitochondrial respiration.[13] The importance of Nrf2 in immunometabolism is also emerging, and it is becoming increasingly recognized that Nrf2, which is activated during metabolic reprogramming in activated macrophages, is critical for resolution of inflammation,[14−16] and that the sensing ability and flexibility of the cysteine sensors in Keap1 are essential for the anti-inflammatory effects of Nrf2 activators.[17] It is therefore not surprising that disturbances in the functions of Nrf2 and/or Keap1 have been implicated in the initiation and progression of most chronic diseases and aging. The Keap1/Nrf2 system is now considered to be a drug target, with a substantial investment by the pharmaceutical industry in the clinical development of Nrf2 modulators.[18]

Key to the regulation of Nrf2 is its interaction with Keap1, which, in addition to serving as a cysteine-based sensor for electrophiles and oxidants,[19,20] is also a substrate adaptor for a Cullin 3-based E3 ubiquitin ligase that continuously targets Nrf2 for ubiquitination and proteasomal degradation.[21−23] Keap1 is a homodimeric protein that binds to the Neh2 domain of monomeric Nrf2 at two motifs: one with low affinity (29-DLG-31) and another with high affinity (79-ETGE-82) (Figure 1A). Both motifs are required for ubiquitination, and the seven lysine residues of Nrf2 that act as ubiquitin acceptors are positioned between these motifs.[24−26] Under unstressed conditions, Nrf2 has a short half-life of about 15−40 min.[27,28] During electrophilic, oxidative, or inflammatory stress, the cysteine sensors in Keap1 are chemically modified.[29−31] Consequently, Keap1 is unable to target Nrf2 for degradation, thereby leading to rapid nuclear accumulation of Nrf2,

DOI: 10.1021/acs.chemrestox.8b00354
Chem. Res. Toxicol. 2019, 32, 500−512

Table 1. Primers Used to Generate Extended Flexible Linkers between Keap1 and mCherry

linker	sequence (peptide)	primer	sequence (DNA)
9fl	RSGKSGEGS	1	CGGGGaaaAGCGGCgaaG
		2	GATCCttcGCCGCTtttCCCCGAT
12fl	RSGKSGSAGEGS	1	CGGGGaaaAGCGGCAGtGcTGGCgaaG
		2	GATCCttcGCCAgCaCTGCCGCTtttCCCCGAT
16fl	RSGKSTGSEGSAGEGS	1	CGGGGaaaAGCactGGTTCAGAAGGCAGtGcTGGCgaaG
		2	GATCCttcGCCAgCaCTGCCTTCTGAACCagtGCTtttCCCCGAT

dimerization with a small musculoaponeurotic fibrosarcoma (sMAF) protein, and activation of Nrf2-target gene transcription. We previously established an imaging-based methodology to visualize and measure the interaction between Nrf2 and Keap1 in single live cells and the effect of small molecule inducers on this interaction.[32] The aim of the research described in this contribution was to improve the existing methodology in order to increase its throughput and precision.

EXPERIMENTAL PROCEDURES

DNA Constructs. Mouse Keap1 in pmCherry-N1 (Keap1−mCherry), mouse Nrf2 in pEGFP-C1 (EGFP−Nrf2), EGFP in mCherry-C1 (EGFP−mCherry), mouse Nrf2 lacking DLG motif in pEGFP-C1 (EGFP-ΔDLG−Nrf2), and mouse Nrf2 with DLG motif replaced by ETGE motif in pEGFP-C1 (EGFP-2xETGE−Nrf2), as well as pEGFP-C1 and pmCherry-N1 (both from Clontech) were previously described.[32] sfGFP-C1 was purchased from Addgene (N54579). The Keap1−6fl-mCherry construct was generated by PCR mutagenesis of the above Keap1−mCherry plasmid using the Quick-Change II site-directed mutagenesis kit (Agilent technologies) and primers ctgtacctgcCGATCGagtactGGATCCATGG-TGAGCAAGGGCG and CGCCCTTGCTCACCATGGATCC-agtactCGATCGgcaggtacag (Eurofins) designed to replace the linker between Keap1 and mCherry by CGATCGagtactGGATCC sequence that codes for a six amino-acid-long flexible RSSTGS linker and introduces unique PvuI, ScaI, and *Bam*HI restriction sites. Mutagenized plasmids were treated with DpnI to remove the old template and introduced into chemicompetent DH10B bacteria that were propagated on LB plates and in LB media in the presence of kanamycin. DNA was isolated using Qiaprep spin miniprep kit (Qiagen). The mutagenesis was confirmed by a diagnostic digest (i.e., the plasmid was linearized with *Bam*HI) followed by sequencing. The Keap1−9fl−mCherry, Keap1−12fl−mCherry, and Keap1−16fl−mCherry constructs were generated by inserting a linker sequence encoded by an annealed pair of the corresponding primers (Eurofin) shown in Table 1 into the PvuI and *Bam*HI sites of the above Keap1−6fl−mCherry construct. The chemicompetent DH10B bacteria transformed by the produced constructs were plated on kanamycin containing LB plates, and colonies were screened for the loss of ScaI restriction site that indicated a successful linker replacement that was further confirmed by sequencing. Mouse Nrf2 in sfGFP-C1 (sfGFP−Nrf2), mouse Nrf2 lacking the DLG motif in sfGFP-C1 (sfGFP-ΔDLG−Nrf2), and mouse Nrf2 with the DLG motif replaced by a second ETGE motif in sfGFP-C1 (sfGFP-2xETGE−Nrf2) were generated by replacing the EGFP sequence between AgeI and BsrGI restriction sites in EGFP−Nrf2, EGFP-ΔDLG−Nrf2, and EGFP-2xETGE−Nrf2 constructs with the corresponding sfGFP sequence obtained from AgeI/BsrGI-mediated restriction digest of sfGFP-C1.

Cells and Treatments. HeLa and HEK293 cells were cultured in DMEM medium supplemented with 10% heat-inactivated fetal bovine serum (FBS). For immunoblots, 4×10^5 cells were plated into each well of a six-well plate 1 day before DNA transfection using lipofectamine 2000 (Invitrogen) and harvested at least 24 h after transfection. For microscopy, 2×10^5 cells were seeded onto glass-bottom 3.5 cm cell culture dishes (FluoroDish, World Precision Instruments) 1 day before DNA transfection using the calcium phosphate method, in phenol-free DMEM supplemented with 10% heat-inactivated FBS, and imaged the day after transfection.

Immunoblotting. Cells were washed twice in PBS and lysed in SDS lysis buffer containing 2% SDS, 62.5 mM Tris-HCl (pH 6.8), 10% glycerol, and cOmplete Mini EDTA-free protease inhibitors (Roche Diagnostics); boiled for 3 min; sonicated using a Sonics Vibra-Cell Ultrasonic processor to shear DNA; and supplemented with DTT (up to 0.1 M) and bromophenol blue. Cell lysate proteins (10 μg) and the PageRuler prestained protein ladder (ThermoFisher Scientific, 26616) were resolved on precast Bis-Tris 4−12% polyacrylamide gel (ThermoFisher Scientific) under a MOPS running buffer and transferred onto a Protran 0.45 μm nitrocellulose blotting membrane (GE Healthcare Life Sciences) in transfer buffer containing 192 mM glycine, 25 mM Tris, and 20% methanol. The membrane was stained with 0.1% Ponceau S in 0.5% acetic acid, destained in 0.5% acetic acid, and scanned using a BioRad ChemiDoc MP Imaging system operated with Image Lab software (BioRad). After rinsing with PBS (Oxoid Phosphate Buffered Saline, Dulbecco A, ThermoFisher, BR0014G), the membrane was blocked for 1 h in blocking solution containing 5% nonfat milk in PBS with 0.1% Tween 20. The blocked membrane was incubated either overnight at 4 °C or for 1−4 h at room temperature with the appropriate primary antibodies that had been diluted in blocking solution. The membrane was washed three times in PBS with 0.1% Tween 20 and incubated for 1 h with the appropriate IRDye-680RD or IRDye-800CW labeled anti-rabbit or anti-mouse secondary antibody (LiCOR), diluted 1:15000 in blocking solution. After three washes in PBS with 0.1% Tween 20, the membrane was scanned using the Odyssey CLx Imaging System (LiCOR). The following primary antibodies were used: rabbit anti−Nrf2 (Cell Signaling Technologies, D1Z9C, 12721P, 1:1000 dilution), rabbit polyclonal anti-EGFP (Abcam, ab6556, 1:1000 dilution) that detects both EGFP and sfGFP, rabbit polyclonal anti-Keap1 [a kind gift from John Hayes (University of Dundee), 1:2000 dilution],[26] and mouse monoclonal anti-β-actin (Sigma, clone AC-15, A 5441, clone AC-15, 1:20 000 dilution).

Live Cell Imaging. Cells were imaged using a confocal Zeiss LSM 710 microscope, operated with ZEN software (Zeiss), equipped with a dark environmental chamber that maintains the temperature at 37 °C and with a supply of humidified 5% CO_2 to the cells. Cells were imaged with 488 and 594 nm confocal lasers for EGFP/sfGFP and mCherry, respectively, with a 63×/1.4NA oil immersion objective, immediately prior to fluorescence lifetime imaging (FLIM) of the same field of view (see below). The acquisition settings for confocal imaging were kept consistent throughout the study, with low power/gain to avoid saturation of bright areas and high averaging to increase signal-to-noise ratio within dim areas.

FLIM Measurements. The time-domain FLIM was measured using a SPC-150 Time-Correlated Single Photon Counter (TCSPC) module (Becker & Hickl) operated with SPCM software (Becker & Hickl). The two-photon laser (Coherent Chameleon) integrated with a Zeiss 710 microscope and operated with ZEN software generated the required pulsed illumination with a repetition rate of 80 MHz and pulse width of 140 fs. For EGFP and sfGFP excitation, the wavelength was set to 920 nm, and the emitted light was directed through 690 SP and 525 ± 25 BP filters to the HPM-100-40GaAsP detector connected to the TCSPC module. The data were collected with laser power adjusted to 0.8×10^5 − 8×10^5 events per second as detected by the Constant Fraction Discriminator (CFD) within TCSPC, for 2 min, with a spatial resolution of 512 × 512 pixels and a time resolution of 256 time channels per curve. The output.sdt files were imported into SPCImage software (Becker & Hickl) for analysis.

DOI: 10.1021/acs.chemrestox.8b00354
Chem. Res. Toxicol. 2019, 32, 500−512

Image Analysis. The images of EGFP, sfGFP, or mCherry fluorescence generated in ZEN software were stored and processed in OMERO.[33] The mean fluorescence intensities within outlined nuclear or cytoplasmic regions of cells were determined using the ROI tool in OMERO.insight. The mean intensity of the background measured in several regions that did not contain cells was further subtracted from the fluorescence intensity data.

The fluorescence lifetime analysis was performed in the SPCImage software (version 5 or 6, see Figure S1), within the region of interest (normally outlining either the nucleus or the cytoplasm of the imaged cell), using an indicated level of spatial binning (n) that pools the data from $(2n + 1) \times (2n + 1)$ adjacent pixels into a single data set, or using global binning (see Figure S2A) that pools the data from the entire region of interest into one data set. Fluorescence lifetime(s) in such data sets is(are) determined by computational fitting of the multi-exponential decay model:

$$F(t) = ae^{-t/\tau} \text{ for one component decay} \quad (A1)$$

$$F(t) = a_1e^{-t/\tau_1} + a_2e^{-t/\tau_2} \text{ for two component decay} \quad (A2)$$

$$F(t) = a_1e^{-t/\tau_1} + a_2e^{-t/\tau_2} + a_3e^{-t/\tau_3} \text{ for three component decay} \quad (A3)$$

where τ_1, τ_2, and τ_3 are the fluorescence lifetimes and a_1, a_2, and a_3 are the amplitude coefficients of the individual components contributing to the total decay function $F(t)$.

Alternatively, in cases when the fluorescence decay is too slow to be completed within a single pulse period, the incomplete decay model that includes the contribution from the previous excitation pulse is used:

$$F_{\text{incomplete}}(t) = F(t) + \sum_{i=1}^{N}\left(a_ie^{-t/\tau_i}\sum_{n=1}^{M}e^{-nT/\tau_i}\right) \quad (B)$$

where M and T are the number and the length of the previous excitation cycles as described in the SPCImage 5.0 manual (2015).

For single-component analysis, the obtained fluorescence lifetime value is

$$tm = \tau$$

while two-component analysis generates two contributing fluorescence lifetimes $t_1 = \tau_1$ and $t_2 = \tau_2$, the relative amplitudes a_1 and a_2, as well as the average lifetime $tm = \tau_m$:

$$\tau_m = \frac{\sum_{i=1}^{N} a_i\tau_i}{\sum_{i=1}^{N} a_i} \quad (C)$$

The fitting algorithm is in-built in SPCImage and incorporates multiple user-defined parameters, including the choice of the model and the number of components in the model. As part of the analytical routine, the instrument response function (IRF, the signal generated by the instrument itself) is removed from the primary data by deconvolution. IRF was either estimated automatically within SPCImage software (the detailed algorithm is provided in the sixth edition of the bh TCSPC Handbook by Wofgang Becker; Figure S2B) or measured as described.[34] Briefly, the decay profile of 10 nm gold nanorods (Sigma 716820), which have a negligibly short luminescence lifetime, was measured at 920 nm, and the photon trace curve generated by global binning of these measurements was used as the IRF curve (Figure S2C). The temporal shift between the used IRF curve and the actual start of IRF ("shift") in the measured region was fixed at the value that was either determined empirically (by accepting the most frequent value fitted by the software in individual pixels) or obtained from a data set generated by the global binning of the entire region by fitting. In the analysis of globally binned areas, the "shift" was left unfixed. The same was done with the offset, except it was fixed at zero if the incomplete decay model was used. Scatter was either fixed at zero or left unfixed (for globally binned data). The data were analyzed with one or two component decay models as indicated. The goodness of fit displayed by the SPCImage software (Figures S1 and S2) was used to choose between "standard" (A) or incomplete (B) decay models.

For measuring FRET efficiency, the two-component decay model was used. In this simplified scenario, the total fluorescence decay in each measured region was regarded as a combination of the fluorescence decays of the unquenched donor molecules (with fluorescence lifetime unaffected by the FRET) and of the quenched donor molecules (with fluorescence lifetime reduced by FRET to a single discrete value due to the proximity of the acceptor). On the basis of these assumptions, we fixed the t_2 value (the larger of the two fluorescence lifetime components) to the value of fluorescence lifetime of the donor in the absence of acceptor and determined t_1 (fluorescence lifetime of quenched donor) and the relative amplitudes a_1 and a_2 via the two-component decay fitting (eq A2). Average fluorescence lifetime tm derived as in eq C was then used within SPCImage to calculate FRET efficiency using the formula

$$E_{\text{FRET}} = 1 - tm/t2 \quad (D)$$

The above fixed t_2 value was obtained separately from measuring the fluorescence lifetime in cells overexpressing EGFP−Nrf2 or sfGFP−Nrf2 without an acceptor.

Numerical data from fluorescence intensities and fluorescence lifetime measurements were compiled in Excel spreadsheets and analyzed in R or in Excel. Scatterplots and the linear regression fitting were made in R.

Statistical Analysis. Mean and standard deviations were calculated either in Excel or in R. For correlation analysis, the Pearson's correlation coefficient, p values for Pearson correlation, the R^2, and the slope of the fitted linear regression functions were obtained in R. For comparison between groups, p values were determined using a Wilcoxon rank sum test or Welch two sample t test in R.

RESULTS AND DISCUSSION

Limitations of the Existing Methodology for Monitoring the Nrf2−Keap1 Interaction in Single Live Cells. The binding between ectopically coexpressed Nrf2 and Keap1 proteins fused to EGFP and mCherry, respectively, at the sites proximal to their interaction interface (the N-terminus of Nrf2 and the C-terminus of Keap1) induces a nonradiative energy transfer, termed Förster Resonance Energy Transfer (FRET), between the EGFP and mCherry fluorophores (Figure 1A). This in turn causes a reduction in the fluorescence lifetime, the time between excitation and emission, of the FRET donor, EGFP. The FRET efficiency (E_{FRET}) calculated as the relative loss of donor fluorescence lifetime in the presence of acceptor (eq 1) provides a measure of the interaction:

$$E_{\text{FRET}} = 1 - t(\text{DA})/t(\text{D}) \quad (1)$$

where t(DA) is the donor fluorescence lifetime in the presence of an acceptor and t(D) is the donor fluorescence lifetime in the absence of an acceptor.[35]

An example of such analysis is given in Figure 1B. Using time-domain Fluorescence Lifetime Imaging Microscopy (FLIM), the fluorescence lifetimes (middle panels) and their corresponding FRET efficiencies (right panels) are determined in each pixel of the image of cells cotransfected with EGFP-labeled Nrf2 and either mCherry-labeled Keap1 (bottom panels) or free mCherry (top panels), which was used as a negative control. The interaction between Keap1 and Nrf2 is apparent from the shorter fluorescence lifetime (tm) of EGFP and the higher FRET efficiency values in the presence of Keap1−mCherry, compared to mCherry. Notably, Keap1−mCherry efficiently retains EGFP−Nrf2 in the cytoplasm, whereas in the absence of Keap1−mCherry, the overexpressed EGFP−Nrf2 is nuclear (Figure 1B, left panels). Using this method, it is possible to examine the steady-state level of the Keap1−Nrf2 interaction in

DOI: 10.1021/acs.chemrestox.8b00354
Chem. Res. Toxicol. 2019, 32, 500−512

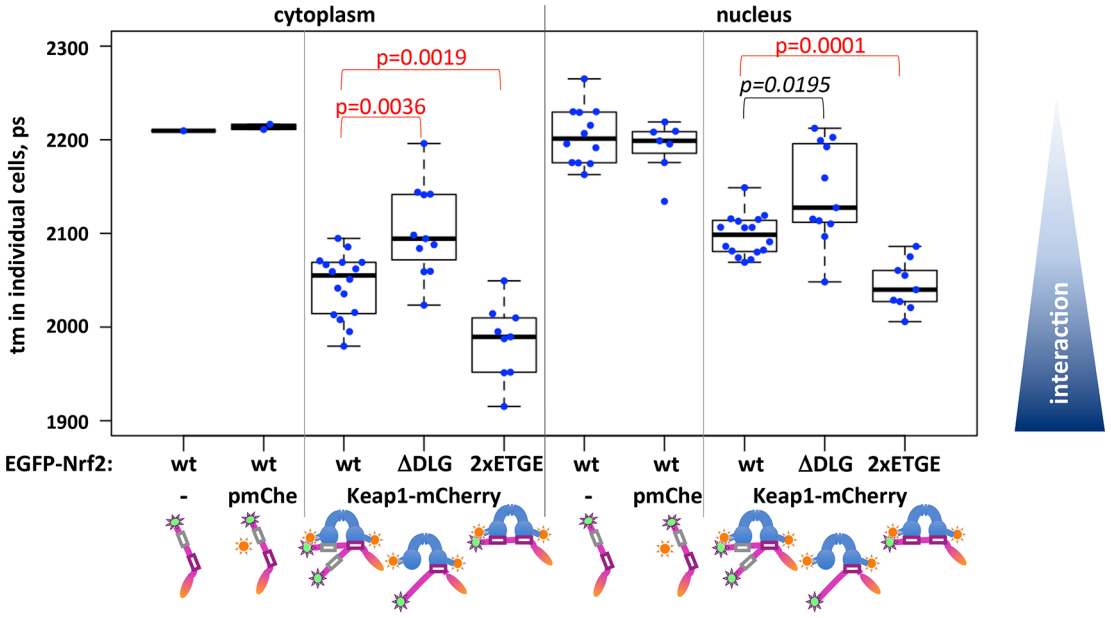

Figure 2. Analysis of the Keap1−Nrf2 interaction using global binning. HEK293 cells were transfected with plasmids encoding wild-type EGFP−Nrf2 or the EGFP−Nrf2 mutant with either lower (ΔDLG) or higher (2xETGE) affinity for Keap1, either alone or together with mCherry or Keap1−mCherry, and subjected to FLIM. The EGFP fluorescence lifetime (*tm*) was analyzed in the cytoplasmic and nuclear areas of the imaged cells, by fitting an incomplete one-exponential decay model to data sets generated by global binning of the data from such areas. Each dot represents the *tm* value in either the nucleus or the cytoplasm of an individual cell; 7−16 cells were measured for each type of transfection. The box plots show the distribution of values within each group of identically transfected cells: the box outlines the range between the 25th and 75th percentiles, the thick line within the box marks the median, and the whiskers show minimum and maximum values that extend from the box by no more than 1.5 times interquartile range (the distance between the 25th and 75th percentiles). The *p* values for significant (black) and highly significant (red) difference in *tm* between groups are shown. Note that lower *tm* indicates a stronger Nrf2−Keap1 interaction.

different cellular regions and observe how Nrf2 inducers change this interaction in real time.[32,36,37] However, high cell-to-cell variability, combined with the extremely low throughput of both measurement and analysis, represent major limitations. Therefore, we set out to improve the current methodology.

Increasing Throughput by Global Binning. First, we made adjustments to the analytical routine with the aim to both simplify it and increase its accuracy. In time-domain FLIM, the fluorescence lifetime value, *tm*, in a given pixel of an image is obtained by a computational fitting of the exponential decay model to a data set that contains experimentally measured times of photon emission, relative to the time of excitation (Figure S1 and Image Analysis within Experimental Procedures). The accuracy of fitting strongly depends on the number of detected photons that accumulate over multiple pulses of laser illumination. Whereas the number of photons could be increased theoretically by extending the duration of acquisition or by increasing the power of the laser, the live cell imaging imposes strict limitations on both of these parameters, due to cell movement and phototoxicity. It is, however, possible to increase the size of the data set by combining the data from several adjacent pixels into one set, a process termed binning, at the expense of spatial resolution. This approach reduced the uncertainty in the fitted *tm* values, as evidenced by the decrease in the standard deviation of the *tm* value among pixels, and removed the bias that lowers the mean *tm* values when the photon number is insufficient (Figure 1C). An extreme case of binning, referred to further as "global binning," combines all data of the entire cellular region of interest into one data set (Figures 1C and S2A). We have previously observed relatively homogenous EGFP-Nrf2 fluorescence lifetimes within either the nucleus or the cytoplasm, and thus do not anticipate an increase in the complexity of the samples upon binning of the entire nuclear or cytoplasmic area into a single data set. Notably, the high number of photons obtained using this approach allows confident fitting of the multiexponential decay function even in dim areas of the image (Figure S2). The increased analytical power is sufficient to computationally fit additional parameters that are otherwise manually (and somewhat arbitrarily) fixed by the user, such as temporal shift of the signal generated by the instrument (the instrument response function, IRF) relative to the start of the data curve, the offset, and the scatter, all of which increase the precision of the analysis. Furthermore, the global binning approach offers a one-step, virtually instantaneous analysis that greatly increases the throughput. Importantly, we confirmed a strong correlation between *tm* obtained from the analysis of globally binned data and mean *tm* from pixel-by-pixel analysis of the same areas of the cells (Figure 1D). Thus, whereas globally binned data are unable to report on the variability within the measured region of interest, they provide a useful measure that represents such regions in studies that address cell-to-cell variability.

Improving Precision by Use of Measured Instrument Response Function. The precision of the measurements was further improved by using the measured IRF in the analysis of FLIM data. The IRF signal is separated and removed from the decay data by deconvolution prior to data analysis within the FLIM analysis software. The SPCImage software allows the generation of a synthetic IRF profile from the shape of the rising edge of the fluorescence signal, and we previously used such estimated IRF in our analysis[32] (Figure S2B). Here, we determined and used the real shape of the IRF curve by measuring the decay profile of ultrafast luminescence of gold nanorods at the wavelength used for EGFP acquisition[34] (Figure

DOI: 10.1021/acs.chemrestox.8b00354
Chem. Res. Toxicol. 2019, 32, 500−512

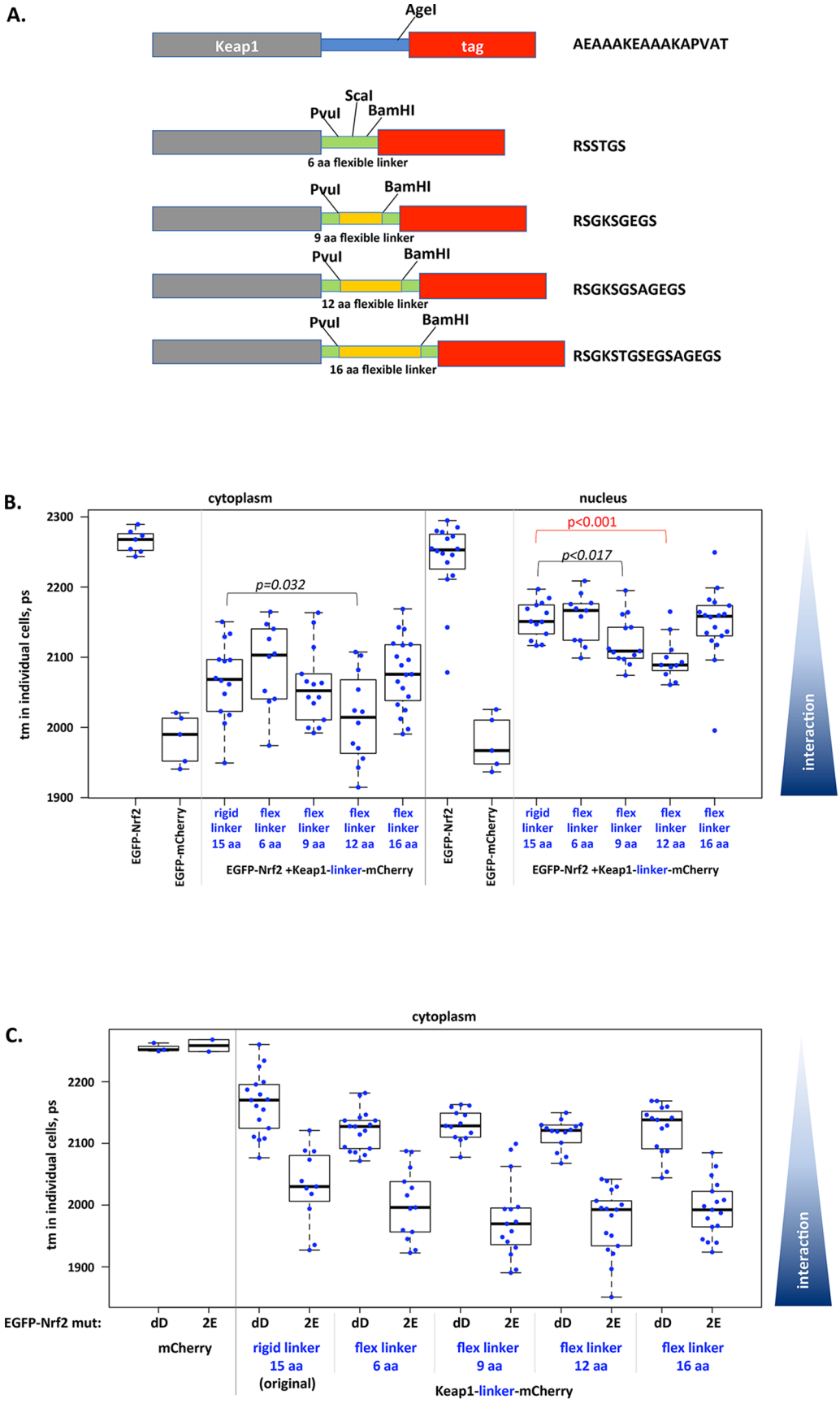

Figure 3. continued

DOI: 10.1021/acs.chemrestox.8b00354
Chem. Res. Toxicol. 2019, 32, 500−512

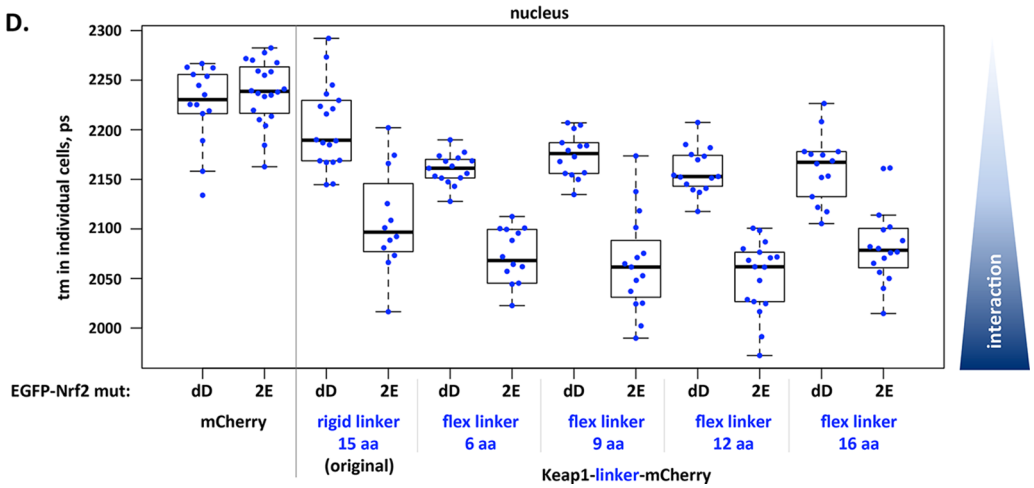

Figure 3. Optimization of the linker between Keap1 and mCherry. (A) Cloning strategy. The top drawing depicts the existing construct with the rigid linker (blue) between the Keap1 (gray rectangle) and the mCherry tag (red rectangle). The construct underneath is cloned by replacing the linker with a short, six-amino-acid flexible linker (green); its DNA sequence incorporated three unique restriction sites. PvuI and *Bam*HI sites were further used to facilitate replacement of this linker by flexible linkers of an increasing length (9-, 12-, or 16-amino-acid-long, bottom three schematics), while the ScaI served as a site for diagnostic digest to detect such a replacement, as it was absent in any further linker sequence. The amino acid sequences of the corresponding linkers are shown on the right. (B) HEK293 cells transfected with EGFP−Nrf2 alone or in the presence of one of the Keap1−mCherry constructs outlined in A. The EGFP fluorescence lifetime (*tm*) was measured, analyzed, and represented as in Figure 2 in the nuclear and cytoplasmic areas of 7−19 cells per group. In addition, cells transfected with EGFP−mCherry construct serving as the "maximal FRET" control were included in the measurements. (C and D) Live FLIM analysis of HEK293 cells transfected with ΔDLG (dD) and 2xETGE (2E) Nrf2 mutants fused to EGFP, with or without the Keap1−mCherry constructs shown in A. The EGFP fluorescence lifetime (*tm*) was measured, analyzed, and represented as in Figure 2 in the cytoplasmic (C) or the nuclear (D) areas.

S2C). This significantly increased the goodness of fit in our analysis (note the decrease in χ^2 in Figure S2C compared to Figure S2B).

Using the Optimized Parameters to Analyze the Nrf2−Keap1 Interaction. The global binning approach was applied to analyze the Nrf2−Keap1 interaction in the entire cytoplasm or the entire nucleus. For simplicity, we used a single-exponential fitting, however the two-exponential decay analysis showed a very similar trend, regardless of whether the complete or incomplete decay model was used (Figure S3). This analysis revealed a robust reduction in *tm* in cells coexpressing EGFP−Nrf2 and Keap1−mCherry in comparison with cells expressing either EGFP−Nrf2 alone or coexpressing EGFP−Nrf2 and free mCherry, indicative of FRET due to the Nrf2−Keap1 interaction (Figure 2). This confirmed our previous results for the cytoplasm[32] and further revealed the occurrence of a similar interaction in the nucleus. Moreover, the reduction in *tm* was significantly smaller in cells coexpressing Keap1−mCherry and the EGFP−Nrf2 mutant that lacks the weak Keap1-binding motif DLG (ΔDLG−Nrf2), indicating a weaker interaction, in agreement with the reduced affinity of this Nrf2 mutant for Keap1.[24] Conversely, the reduction in *tm* was greater in cells coexpressing Keap1−mCherry and the EGFP−Nrf2 mutant, in which the DLG motif was replaced with the strong Keap1-binding motif ETGE (2xETGE−Nrf2), indicating a stronger interaction. Notably, the interactions between the fusion proteins showed a similar pattern in both the cytoplasm and the nucleus.

Optimizing the Linker between Keap1 and mCherry. To further increase the sensitivity of the assay and to rule out potential orientation bias in our system, we next optimized the linker between Keap1 and mCherry. Since FRET is sensitive to the mutual orientation of the fluorophores,[38] the changes in conformation of the protein complex that affect fluorophore orientation could alter FRET efficiency and complicate its interpretation. For intermolecular FRET to report primarily on the interaction strength (i.e., distance between partners and/or frequency of interaction), the flexible linkers[39] between proteins and their fluorescent tags are preferable. The existing linker between Keap1 and mCherry, AEAAAKEAAAKAPVAT (Figure 3A, top), forms a rigid two-turn helix that may introduce an unwanted bias toward a particular geometrical configuration of the complex. We first replaced the rigid linker with a short six-amino acid flexible linker that incorporated three restriction sites for the ease of further mutagenesis (Figure 3A, second construct from top). We then generated a series of Keap1−mCherry constructs with flexible linkers of increasing length (Figure 3A). While the Keap1−mCherry construct with a six-amino-acid flexible linker shortened the fluorescence lifetime of EGFP−Nrf2 to a similar extent as the original Keap1−mCherry construct, a further increase in the linker length, up to 12 amino acids, gradually enhanced its FRET capacity, which decreased again when the size of the flexible linker was extended to 16 amino acids (Figure 3B). Analysis of the interaction between both ΔDLG and 2xETGE EGFP−Nrf2 mutants and the Keap1−mCherry constructs containing flexible linkers of different sizes revealed that all of them were able to discriminate between those mutants of Nrf2 (Figure 3C and D), confirming that the difference in FRET efficiency between Nrf2 mutants is not due to an orientation bias of the original Keap1−mCherry construct.

Since the construct with the 12 amino acid flexible linker was the most efficient in mediating FRET, we used this Keap1−mCherry construct (designated Keap1−12fl−mChe) in our subsequent experiments. The sensitivity of this construct combined with the above analytical routine was further tested on samples that coexpressed high-affinity and low-affinity EGFP-labeled Nrf2 mutants at different ratios (Figure S4). The Keap1−Nrf2 interaction was significantly weaker in cells expressing a mixture of ΔDLG−Nrf2 and 2xETGE−Nrf2 at 1:2

DOI: 10.1021/acs.chemrestox.8b00354
Chem. Res. Toxicol. 2019, 32, 500−512

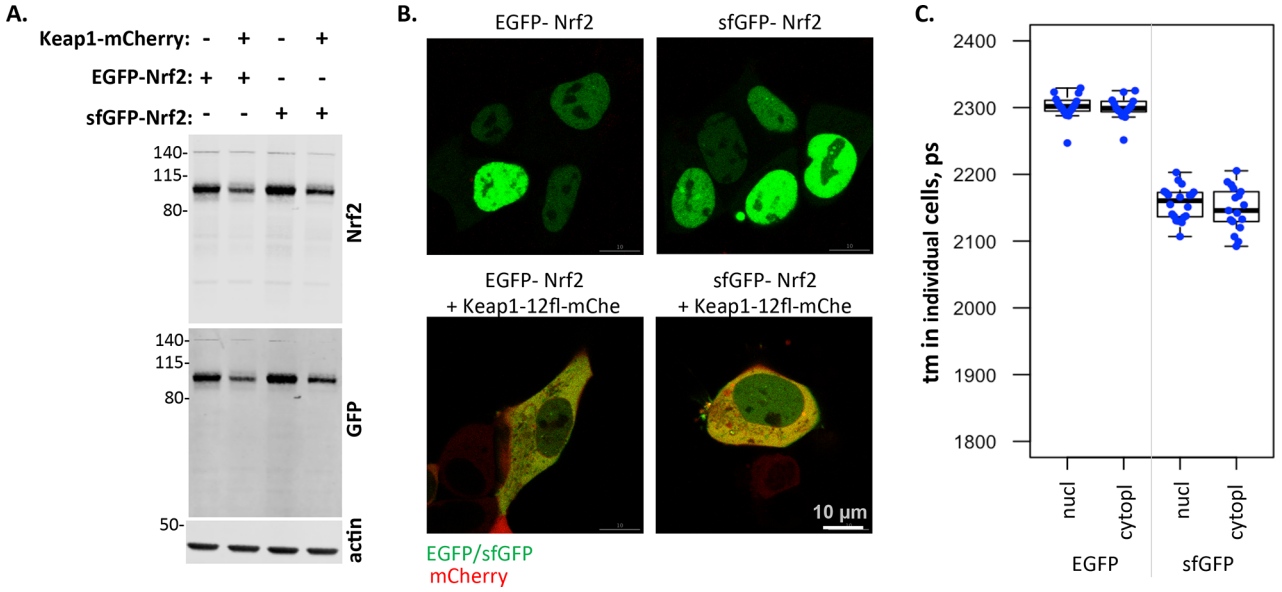

Figure 4. Assessment of the sfGFP tag. (A) sfGFP−Nrf2 and EGFP−Nrf2 have similar expression levels and the ability to be degraded by Keap1−mCherry. HEK293 cells transfected for 1 day with either sfGFP- or EGFP-tagged Nrf2, either alone or together with Keap1−mCherry, were lysed and immunoblotted for Nrf2, GFP, and actin (as a loading control). (B) The cellular localization of sfGFP−Nrf2 and EGFP−Nrf2 is identical. HEK293 transfected with Nrf2 tagged with either EGFP (left) or sfGFP (right), with (bottom) or without (top) Keap1−12fl−mCherry were imaged using confocal microscopy to detect EGFP/sfGFP that have identical fluorescence spectra (green in overlay) or mCherry (red in overlay). Note that the nuclear localization of both tagged versions of Nrf2 is changed to predominantly cytoplasmic when Keap1−mCherry is coexpressed. (C) The fluorescence lifetime (*tm*) of sfGFP and EGFP was measured in live HEK293 cells transfected with the corresponding construct. The data were analyzed and are represented as in Figure 2. Note that the *tm* of sfGFP is slightly lower and noisier than that of EGFP.

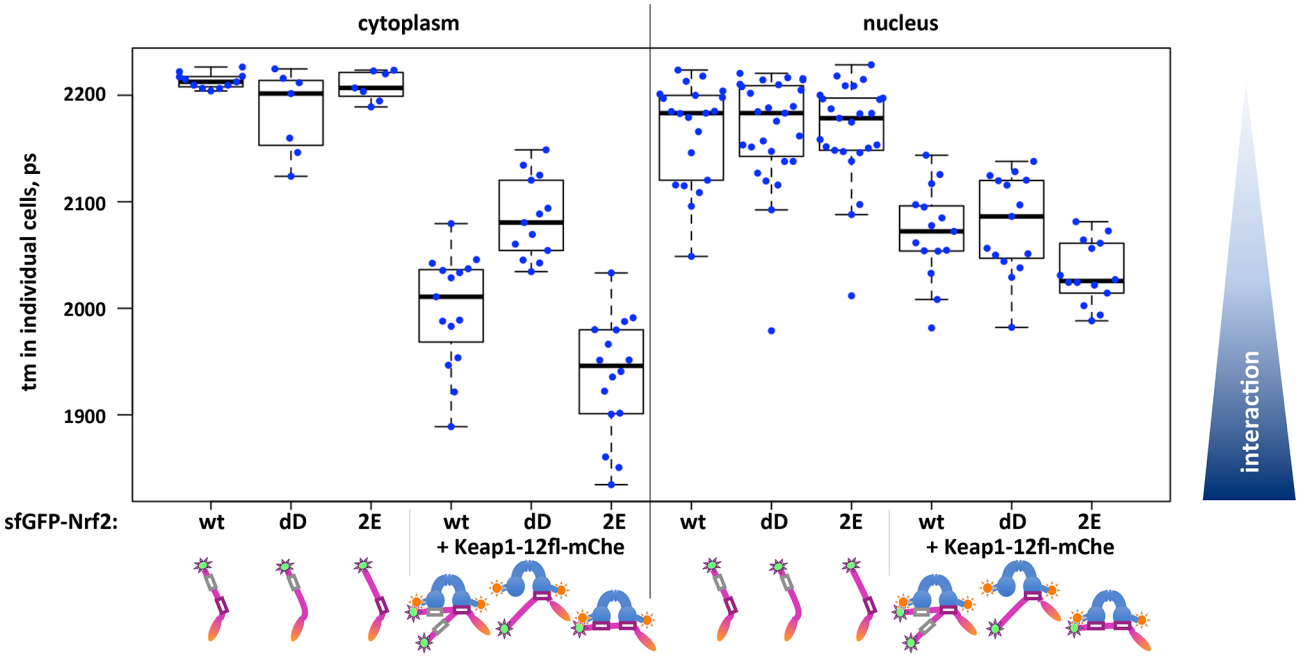

Figure 5. sfGFP is a good FRET donor for the FLIM−FRET Nrf2−Keap1 interaction assay. HEK293 cells were transfected with wild-type sfGFP−Nrf2 or sfGFP−Nrf2 mutant with either lower (ΔDLG, dD) or higher (2xETGE, 2E) affinity for Keap1, either alone or together with Keap1−12fl−mCherry, and subjected to FLIM. The sfGFP fluorescence lifetime (*tm*) in the cytoplasmic and nuclear areas of the imaged cells was analyzed and presented as in Figure 2.

ratio compared to those expressing 2xETGE−Nrf2 alone, and this was further reduced at a ΔDLG−Nrf2 and 2xETGE−Nrf2 ratio of 2:1. This observation demonstrates that the method is suitable for the detection of subtle changes in the ability of Nrf2 to bind Keap1 even in samples with complex composition.

Matching the Maturation Time of the Fluorescent Protein Tag to the Half-Life of Nrf2. One of the obstacles in using the existing method was fast degradation of FRET-donor-labeled Nrf2, particularly in the presence of Keap1. Nrf2 is a very short-lived protein, with a half-life of about 15−40 min, depending on the cell line.[27,28] Since the maturation time of

DOI: 10.1021/acs.chemrestox.8b00354
Chem. Res. Toxicol. 2019, 32, 500−512

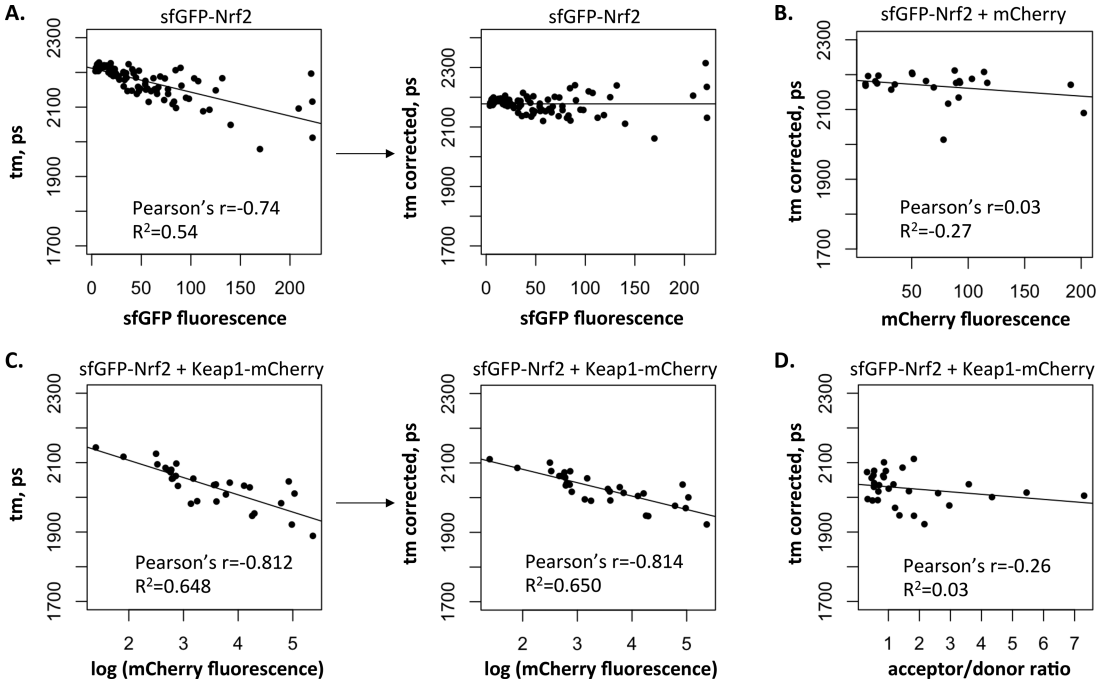

Figure 6. Contribution of GFP and mCherry intensities to the cell-to-cell variability in the GFP fluorescence lifetime. (A) The sfGFP fluorescence lifetime (*tm*) determined using a one-exponential decay model with global binning in the nuclear or cytoplasmic regions of HEK293 cells expressing sfGFP−Nrf2 (wild-type or mutants) was plotted against the mean sfGFP intensity measured in the same regions of the cell. Fitting the linear regression to the data confirmed the correlation between *tm* and sfGFP fluorescence level (Pearson's coefficient and adjusted R^2 are shown on the plot, left panel). On the basis of the slope of the linear regression line (slope = −0.6894), the *tm* for each data point was further corrected for the sfGFP intensity using the formula: *tm* corrected = *tm* + [0.6894 × (sfGFP intensity − 50)]. The corrected *tm* values plotted against the sfGFP intensity for the same data set (right panel) revealed complete correction, apparent from the lack of slope in the fitted linear regression. (B) sfGFP fluorescence lifetime measured in the nuclear or cytoplasmic regions of HEK293 cells coexpressing sfGFP−Nrf2 and free mCherry corrected as in A (*tm* corrected) was plotted against the mean fluorescence level of mCherry. The Pearson's coefficient, the adjusted R^2 value (shown on the plot), and the lack of slope of the fitted linear regression confirm the lack of correlation between the plotted values. (C) Correlation between sfGFP fluorescence lifetime in the nuclear or cytoplasmic regions of HEK293 cells coexpressing sfGFP−Nrf2 and Keap1−12fl−mCherry measured as in A and the logarithm of the mean mCherry fluorescence, without (left panel) and with (right panel) correction for sfGFP fluorescence as in A, is apparent from the slope of the fitted linear regression and the corresponding Pearson's coefficient and adjusted R^2 values as shown. (D) No correlation between the corrected *tm* and the ratio between acceptor and donor in the sample coexpressing sfGFP−Nrf2 and Keap1−mCherry. Corrected *tm* values in the same data set as in C were plotted against the ratio between mCherry and sfGFP fluorescence intensities. Fitted linear regression, Pearson's coefficient, and adjusted R^2 are shown.

EGFP (the time from synthesis to the onset of fluorescence) is more than 30 min,[40] a significant proportion of EGFP−Nrf2 is likely to degrade before it becomes detectable. Therefore, the obtained data might not fully represent the bulk of Nrf2 behavior. In order to overcome this limitation, we replaced EGFP in EGFP−Nrf2 with superfolder GFP (sfGFP),[41] which has fluorescence spectra very similar to EGFP but a much faster maturation time, 6−7 min.[42] Coexpression with Keap1−mCherry led to an identical decrease in the levels of ectopically expressed sfGFP−Nrf2 as those of EGFP−Nrf2 (Figure 4A). The localization of sfGFP−Nrf2 ectopically expressed in HEK293 (Figure 4B) or HeLa cells (not shown) was indistinguishable from that of EGFP−Nrf2, either in the presence or in the absence of Keap1−mCherry. The fluorescence lifetime of sfGFP in cells was 2156 ± 25 ps in cytoplasmic and 2148 ± 33 ps in nuclear regions (Figure 4C), slightly shorter and more variable than that of EGFP. FRET between sfGFP−Nrf2 and Keap1−12fl−mCherry was detected in both the cytoplasm and the nucleus (Figure 5), and in the cytoplasm, there was a clear and significant difference in the level of Keap1 interaction between wild-type Nrf2 and ΔDLG or 2xETGE Nrf2 mutants labeled with sfGFP. Collectively, these data strongly suggest that sfGFP−Nrf2 and EGFP−Nrf2 interact with Keap1−mCherry in the same manner. Furthermore, the fluorescence intensity of the sfGFP−Nrf2 expressing cells was greatly increased in comparison to EGFP−Nrf2 expressing cells, which increased both the speed of the measurements and the representability of the data. Thus, the sfGFP:mCherry fluorophore pair offers a valid alternative for FRET measurements of short-lived proteins using FLIM.

Identifying the Level of Acceptor As a Contributing Factor to Cell-to-Cell Variability. Another factor that undermines the robustness of the existing assay is high cell-to-cell variability. In order to determine the source of this variability, we analyzed the relationship between the fluorescence intensity of the donor or acceptor and the fluorescence lifetime of the donor, within each group. For cells expressing the sfGFP−Nrf2 donor alone, the fluorescence intensity of sfGFP moderately correlated with *tm* values (Figure 6A, left panel). While the fluorescence lifetime is considered to be independent of the donor concentration,[35] our data indicate that the donor expression level affects the *tm* measurements to some degree. In order to limit the potential effect of homo-FRET[43] that might occur at high fluorophore density, and any artifacts induced by phototoxicity, the brightest cells with extreme levels of overexpressed protein were excluded from this analysis.

DOI: 10.1021/acs.chemrestox.8b00354
Chem. Res. Toxicol. 2019, 32, 500−512

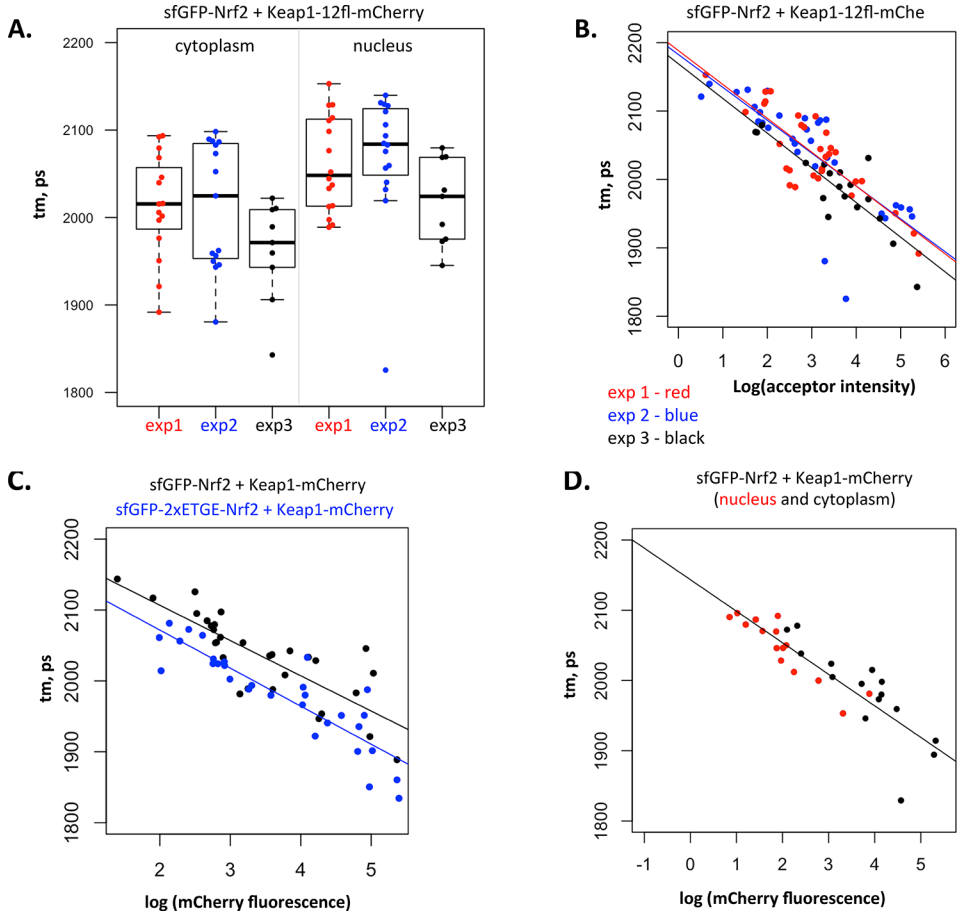

Figure 7. Analysis of the donor fluorescence lifetime in the context of the acceptor level reveals high reproducibility of Nrf2−Keap1 interaction measurements. (A) The sfGFP fluorescence lifetime (*tm*) of cytoplasmic (left) or nuclear (right) regions of HeLa cells cotransfected with sfGFP−Nrf2 and Keap1−12fl−mCherry was measured and analyzed as in Figure 2 in three independent experiments acquired on different days. (B) The same data plotted against the logarithm of mean mCherry intensity measured in the same regions, with linear regressions fitted independently to each experimental data set. The data from experiments 1, 2, and 3 (shown in A) are color-coded as red, blue, and black, respectively. (C) HEK 293 cells transfected with Keap1−12fl−mCherry and either wild-type sfGFP−Nrf2 (black) or mutant sfGFP−Nrf2 in which the low-affinity DLG site was replaced by a second high-affinity ETGE site (sfGFP−2xETGE−Nrf2, blue) were measured and analyzed as in Figure 6C. The corresponding linear regressions were fitted independently to each data set and are similarly color-coded. (D) The sfGFP fluorescence lifetime (*tm*) of the cytoplasmic (black) or nuclear (red) regions of HeLa cells cotransfected with sfGFP−Nrf2 and Keap1−12fl−mCherry were measured and analyzed as in Figure 6C. Linear regression was fitted to the entire data set.

Additionally, in order to prevent the bias toward shorter *tm* due to exclusion of late arriving photons if more than one photon is excited within the same pulse of the laser illumination, the so-called pile-up effect, the acquisition speed was set to maintain the low count rate $0.8 \times 10^5 - 8 \times 10^5$ events per second, corresponding to 0.001−0.01 photons per pulse). However, despite these precautions, the correlation between donor fluorescence lifetime and its total fluorescence level always remained. The same trend was seen with EGFP (Figure S5).

In order to remove the above effect from further analysis, we fitted a linear regression function to the data shown in Figure 6A, left panel, and determined the slope of the regression line. This value was used to calculate the corrected *tm* that takes the total sfGFP intensity into account (Figure 6A, right panel). We further analyzed the effect of free mCherry coexpressed with the donor on the donor fluorescence lifetime. After correction for the level of sfGFP intensity, the sfGFP fluorescence lifetime was not dependent on mCherry fluorescence over a large range of its intensities (Figure 6B), and was only reduced at extremely high levels of mCherry (Figure S6).

However, in cells that coexpressed sfGFP−Nrf2 and Keap1−mCherry, the relationship between *tm* or corrected *tm* with donor and acceptor intensities was more complex (Figure S7 and Table S1). The logarithm of the mean mCherry intensity showed the strongest correlation with sfGFP fluorescence lifetime, based on the Pearson's coefficient and R^2 values, without (Figure 6C, left panel) or with (Figure 6C, right panel) correction for the total sfGFP intensity. One possible explanation for such correlation could be a suboptimal concentration of acceptor in our system, which is dictated by the need to maintain Keap1−mCherry at a relatively low level to avoid degradation of sfGFP−Nrf2 beyond detectable levels (Figure S8). FRET efficiency has been previously shown to be low at the suboptimal concentration of FRET acceptor relative to that of FRET donor, and to increase with the ratio between the FRET acceptor and the FRET donor until it reaches a plateau when the acceptor is in excess over the donor.[44] Surprisingly, we found no correlation between the corrected (Figure 6D) or uncorrected (Figure S7 and Table S1) sfGFP fluorescence lifetime (that is inversely related to FRET efficiency, see formulas D and 1 and Figure 1B) and the ratio

DOI: 10.1021/acs.chemrestox.8b00354
Chem. Res. Toxicol. 2019, 32, 500−512

between acceptor and donor intensities in samples coexpressing sfGFP−Nrf2 and Keap1−12fl-mCherry. Thus, within the range of fluorescence intensities used in our measurements, the absolute level of acceptor attached to the binding partner, rather than the acceptor to donor ratio, is linked to the cell-to-cell variability in the fluorescence lifetime of the FRET donor. It is possible that this unique behavior results from complex multiway dependencies between the efficiency of interaction and the expression levels of EGFP−Nrf2 and Keap1−mCherry.

While the precise reason for the above correlation remains to be determined, we nevertheless decided to utilize it to increase the robustness and sensitivity of the assay, by analyzing the donor fluorescence lifetime in the context of the acceptor level. Such two-dimentional representation revealed a high level of reproducibility of the measurements between experiments (compare Figure 7B with 7A). It could clearly discriminate between wild-type Nrf2 and the 2xETGE−Nrf2 mutant with increased affinity for Keap1 that showed a reduction in *tm* across the entire range of acceptor intensity (Figure 7C), consistent with higher FRET efficiency between the mutant Nrf2 protein and Keap1−12fl−mCherry. Furthermore, inspection of the correlation between *tm* and logarithm of acceptor intensity in different cellular compartments revealed that it does not significantly differ between nuclear and cytoplasmic areas (Figure 7D). This observation suggests that the main cause of the lower FRET efficiency in the nucleus compared to the cytoplasm in our assay (Figures 2, 3B, 5, and 7A) is the low abundance of acceptor, which in turn is caused by the predominant cytoplasmic localization of Keap1 (see Figure 1B),[45] and is not due to differences in the overall affinity of Nrf2 for Keap1 between the two subcellular compartments.

CONCLUDING REMARKS

We have developed an improved imaging-based FLIM/FRET methodology to monitor the interaction between Nrf2 and Keap1 in single live cells, with strongly increased throughput compared to the previously described method. The use of global binning increases the throughput of the assay, and the use of the measured instrument response function in the analysis improves its precision. Incorporating a flexible linker between Keap1 and the FRET acceptor fluorescent protein tag eliminates the possibility of introducing an orientation bias. We showed that sfGFP:mCherry fluorophore combination is an appropriate choice for measuring the FLIM−FRET of short-lived proteins and that matching the maturation time of the donor with the short half-life of Nrf2 improves capture of representative images without any detectable drawbacks. Finally, we identified the level of acceptor as the main factor that correlates with cell-to-cell variability and, more importantly, developed the strategy to eliminate its effect from measurements of the Keap1−Nrf2 interaction.

ASSOCIATED CONTENT

Supporting Information

The Supporting Information is available free of charge on the ACS Publications website at DOI: 10.1021/acs.chemrestox.8b00354.

Figures S1−S8 and Table S1, showing further details of method validation (PDF)

AUTHOR INFORMATION

Corresponding Authors

*E-mail: d.dikovskaya@dundee.ac.uk.
*E-mail: a.dinkovakostova@dundee.ac.uk.

ORCID

Albena T. Dinkova-Kostova: 0000-0003-0316-9859

Notes

The authors declare no competing financial interest.

ACKNOWLEDGMENTS

We thank John Hayes (University of Dundee) for generously providing the anti-Keap1 antibody and Andrew Cassidy (Tayside Centre for Genomic Analysis, University of Dundee) for DNA sequencing. We are grateful to the Biotechnology and Biological Sciences Research Council (BB/L01923X/1), Tenovus Scotland (T17/14), and Cancer Research UK (C20953/A18644) for financial support.

REFERENCES

(1) Hayes, J. D., and Dinkova-Kostova, A. T. (2014) The Nrf2 regulatory network provides an interface between redox and intermediary metabolism. *Trends Biochem. Sci. 39*, 199−218.

(2) Yamamoto, M., Kensler, T. W., and Motohashi, H. (2018) The KEAP1-NRF2 System: a Thiol-Based Sensor-Effector Apparatus for Maintaining Redox Homeostasis. *Physiol. Rev. 98*, 1169−1203.

(3) Kovac, S., Angelova, P. R., Holmstrom, K. M., Zhang, Y., Dinkova-Kostova, A. T., and Abramov, A. Y. (2015) Nrf2 regulates ROS production by mitochondria and NADPH oxidase. *Biochim. Biophys. Acta, Gen. Subj. 1850*, 794−801.

(4) Tanito, M., Agbaga, M. P., and Anderson, R. E. (2007) Upregulation of thioredoxin system via Nrf2-antioxidant responsive element pathway in adaptive-retinal neuroprotection in vivo and in vitro. *Free Radical Biol. Med. 42*, 1838−1850.

(5) MacLeod, A. K., McMahon, M., Plummer, S. M., Higgins, L. G., Penning, T. M., Igarashi, K., and Hayes, J. D. (2009) Characterization of the cancer chemopreventive NRF2-dependent gene battery in human keratinocytes: demonstration that the KEAP1-NRF2 pathway, and not the BACH1-NRF2 pathway, controls cytoprotection against electrophiles as well as redox-cycling compounds. *Carcinogenesis 30*, 1571−1580.

(6) Agyeman, A. S., Chaerkady, R., Shaw, P. G., Davidson, N. E., Visvanathan, K., Pandey, A., and Kensler, T. W. (2012) Transcriptomic and proteomic profiling of KEAP1 disrupted and sulforaphane-treated human breast epithelial cells reveals common expression profiles. *Breast Cancer Res. Treat. 132*, 175−187.

(7) Dinkova-Kostova, A. T., and Talalay, P. (2010) NAD(P)H:quinone acceptor oxidoreductase 1 (NQO1), a multifunctional antioxidant enzyme and exceptionally versatile cytoprotector. *Arch. Biochem. Biophys. 501*, 116−123.

(8) Sedlak, T. W., Saleh, M., Higginson, D. S., Paul, B. D., Juluri, K. R., and Snyder, S. H. (2009) Bilirubin and glutathione have complementary antioxidant and cytoprotective roles. *Proc. Natl. Acad. Sci. U. S. A. 106*, 5171−5176.

(9) Mitsuishi, Y., Taguchi, K., Kawatani, Y., Shibata, T., Nukiwa, T., Aburatani, H., Yamamoto, M., and Motohashi, H. (2012) Nrf2 redirects glucose and glutamine into anabolic pathways in metabolic reprogramming. *Cancer Cell 22*, 66−79.

(10) DeNicola, G. M., Chen, P. H., Mullarky, E., Sudderth, J. A., Hu, Z., Wu, D., Tang, H., Xie, Y., Asara, J. M., Huffman, K. E., Wistuba, II, Minna, J. D., DeBerardinis, R. J., and Cantley, L. C. (2015) NRF2 regulates serine biosynthesis in non-small cell lung cancer. *Nat. Genet. 47*, 1475−1481.

(11) Slocum, S. L., Skoko, J. J., Wakabayashi, N., Aja, S., Yamamoto, M., Kensler, T. W., and Chartoumpekis, D. V. (2016) Keap1/Nrf2 pathway activation leads to a repressed hepatic gluconeogenic and

DOI: 10.1021/acs.chemrestox.8b00354
Chem. Res. Toxicol. 2019, 32, 500−512

lipogenic program in mice on a high-fat diet. *Arch. Biochem. Biophys. 591*, 57−65.
(12) Meakin, P. J., Chowdhry, S., Sharma, R. S., Ashford, F. B., Walsh, S. V., McCrimmon, R. J., Dinkova-Kostova, A. T., Dillon, J. F., Hayes, J. D., and Ashford, M. L. (2014) Susceptibility of Nrf2-Null Mice to Steatohepatitis and Cirrhosis upon Consumption of a High-Fat Diet Is Associated with Oxidative Stress, Perturbation of the Unfolded Protein Response, and Disturbance in the Expression of Metabolic Enzymes but Not with Insulin Resistance. *Mol. Cell. Biol. 34*, 3305−3320.
(13) Holmstrom, K. M., Baird, L., Zhang, Y., Hargreaves, I., Chalasani, A., Land, J. M., Stanyer, L., Yamamoto, M., Dinkova-Kostova, A. T., and Abramov, A. Y. (2013) Nrf2 impacts cellular bioenergetics by controlling substrate availability for mitochondrial respiration. *Biol. Open 2*, 761−770.
(14) Thimmulappa, R. K., Lee, H., Rangasamy, T., Reddy, S. P., Yamamoto, M., Kensler, T. W., and Biswal, S. (2006) Nrf2 is a critical regulator of the innate immune response and survival during experimental sepsis. *J. Clin. Invest. 116*, 984−995.
(15) Mills, E. L., Ryan, D. G., Prag, H. A., Dikovskaya, D., Menon, D., Zaslona, Z., Jedrychowski, M. P., Costa, A. S. H., Higgins, M., Hams, E., Szpyt, J., Runtsch, M. C., King, M. S., McGouran, J. F., Fischer, R., Kessler, B. M., McGettrick, A. F., Hughes, M. M., Carroll, R. G., Booty, L. M., Knatko, E. V., Meakin, P. J., Ashford, M. L. J., Modis, L. K., Brunori, G., Sevin, D. C., Fallon, P. G., Caldwell, S. T., Kunji, E. R. S., Chouchani, E. T., Frezza, C., Dinkova-Kostova, A. T., Hartley, R. C., Murphy, M. P., and O'Neill, L. A. (2018) Itaconate is an anti-inflammatory metabolite that activates Nrf2 via alkylation of KEAP1. *Nature 556*, 113−117.
(16) Olagnier, D., Brandtoft, A. M., Gunderstofte, C., Villadsen, N. L., Krapp, C., Thielke, A. L., Laustsen, A., Peri, S., Hansen, A. L., Bonefeld, L., Thyrsted, J., Bruun, V., Iversen, M. B., Lin, L., Artegoitia, V. M., Su, C., Yang, L., Lin, R., Balachandran, S., Luo, Y., Nyegaard, M., Marrero, B., Goldbach-Mansky, R., Motwani, M., Ryan, D. G., Fitzgerald, K. A., O'Neill, L. A., Hollensen, A. K., Damgaard, C. K., de Paoli, F. V., Bertram, H. C., Jakobsen, M. R., Poulsen, T. B., and Holm, C. K. (2018) Nrf2 negatively regulates STING indicating a link between antiviral sensing and metabolic reprogramming. *Nat. Commun. 9*, 3506.
(17) Dayalan Naidu, S., Muramatsu, A., Saito, R., Asami, S., Honda, T., Hosoya, T., Itoh, K., Yamamoto, M., Suzuki, T., and Dinkova-Kostova, A. T. (2018) C151 in KEAP1 is the main cysteine sensor for the cyanoenone class of NRF2 activators, irrespective of molecular size or shape. *Sci. Rep. 8*, 8037.
(18) Cuadrado, A., Rojo, A. I., Wells, G., Hayes, J. D., Cousin, S. P., Rumsey, W. L., Attucks, O. C., Franklin, S., Levonen, A. L., Kensler, T. W., and Dinkova-Kostova, A. T. (2019) Therapeutic targeting of the NRF2 and KEAP1 partnership in chronic diseases, *Nat. Rev. Drug Discovery*, in press, DOI: 10.1038/s41573-018-0008-x.
(19) Sihvola, V., and Levonen, A. L. (2017) Keap1 as the redox sensor of the antioxidant response. *Arch. Biochem. Biophys. 617*, 94−100.
(20) Dinkova-Kostova, A. T., Kostov, R. V., and Canning, P. (2017) Keap1, the cysteine-based mammalian intracellular sensor for electrophiles and oxidants. *Arch. Biochem. Biophys. 617*, 84−93.
(21) Zhang, D. D., Lo, S. C., Cross, J. V., Templeton, D. J., and Hannink, M. (2004) Keap1 is a redox-regulated substrate adaptor protein for a Cul3-dependent ubiquitin ligase complex. *Mol. Cell. Biol. 24*, 10941−10953.
(22) Cullinan, S. B., Gordan, J. D., Jin, J., Harper, J. W., and Diehl, J. A. (2004) The Keap1-BTB protein is an adaptor that bridges Nrf2 to a Cul3-based E3 ligase: oxidative stress sensing by a Cul3-Keap1 ligase. *Mol. Cell. Biol. 24*, 8477−8486.
(23) Kobayashi, A., Kang, M. I., Okawa, H., Ohtsuji, M., Zenke, Y., Chiba, T., Igarashi, K., and Yamamoto, M. (2004) Oxidative stress sensor Keap1 functions as an adaptor for Cul3-based E3 ligase to regulate proteasomal degradation of Nrf2. *Mol. Cell. Biol. 24*, 7130−7139.
(24) Tong, K. I., Katoh, Y., Kusunoki, H., Itoh, K., Tanaka, T., and Yamamoto, M. (2006) Keap1 recruits Neh2 through binding to ETGE and DLG motifs: characterization of the two-site molecular recognition model. *Mol. Cell. Biol. 26*, 2887−2900.
(25) McMahon, M., Itoh, K., Yamamoto, M., and Hayes, J. D. (2003) Keap1-dependent proteasomal degradation of transcription factor Nrf2 contributes to the negative regulation of antioxidant response element-driven gene expression. *J. Biol. Chem. 278*, 21592−21600.
(26) McMahon, M., Thomas, N., Itoh, K., Yamamoto, M., and Hayes, J. D. (2006) Dimerization of substrate adaptors can facilitate cullin-mediated ubiquitylation of proteins by a "tethering" mechanism: a two-site interaction model for the Nrf2-Keap1 complex. *J. Biol. Chem. 281*, 24756−24768.
(27) McMahon, M., Thomas, N., Itoh, K., Yamamoto, M., and Hayes, J. D. (2004) Redox-regulated turnover of Nrf2 is determined by at least two separate protein domains, the redox-sensitive Neh2 degron and the redox-insensitive Neh6 degron. *J. Biol. Chem. 279*, 31556−31567.
(28) Katoh, Y., Iida, K., Kang, M. I., Kobayashi, A., Mizukami, M., Tong, K. I., McMahon, M., Hayes, J. D., Itoh, K., and Yamamoto, M. (2005) Evolutionary conserved N-terminal domain of Nrf2 is essential for the Keap1-mediated degradation of the protein by proteasome. *Arch. Biochem. Biophys. 433*, 342−350.
(29) Dinkova-Kostova, A. T., Holtzclaw, W. D., Cole, R. N., Itoh, K., Wakabayashi, N., Katoh, Y., Yamamoto, M., and Talalay, P. (2002) Direct evidence that sulfhydryl groups of Keap1 are the sensors regulating induction of phase 2 enzymes that protect against carcinogens and oxidants. *Proc. Natl. Acad. Sci. U. S. A. 99*, 11908−11913.
(30) McMahon, M., Lamont, D. J., Beattie, K. A., and Hayes, J. D. (2010) Keap1 perceives stress via three sensors for the endogenous signaling molecules nitric oxide, zinc, and alkenals. *Proc. Natl. Acad. Sci. U. S. A. 107*, 18838−18843.
(31) Saito, R., Suzuki, T., Hiramoto, K., Asami, S., Naganuma, E., Suda, H., Iso, T., Yamamoto, H., Morita, M., Baird, L., Furusawa, Y., Negishi, T., Ichinose, M., and Yamamoto, M. (2015) Characterizations of Three Major Cysteine Sensors of Keap1 in Stress Response. *Mol. Cell. Biol. 36*, 271−284.
(32) Baird, L., Lleres, D., Swift, S., and Dinkova-Kostova, A. T. (2013) Regulatory flexibility in the Nrf2-mediated stress response is conferred by conformational cycling of the Keap1−Nrf2 protein complex. *Proc. Natl. Acad. Sci. U. S. A. 110*, 15259−15264.
(33) Allan, C., Burel, J. M., Moore, J., Blackburn, C., Linkert, M., Loynton, S., Macdonald, D., Moore, W. J., Neves, C., Patterson, A., Porter, M., Tarkowska, A., Loranger, B., Avondo, J., Lagerstedt, I., Lianas, L., Leo, S., Hands, K., Hay, R. T., Patwardhan, A., Best, C., Kleywegt, G. J., Zanetti, G., and Swedlow, J. R. (2012) OMERO: flexible, model-driven data management for experimental biology. *Nat. Methods 9*, 245−253.
(34) Talbot, C. B., Patalay, R., Munro, I., Warren, S., Ratto, F., Matteini, P., Pini, R., Breunig, H. G., Konig, K., Chu, A. C., Stamp, G. W., Neil, M. A., French, P. M., and Dunsby, C. (2011) Application of ultrafast gold luminescence to measuring the instrument response function for multispectral multiphoton fluorescence lifetime imaging. *Opt. Express 19*, 13848−13861.
(35) Lakowicz, J. R. (2006) *Principles of Fluorescence Spectroscopy*, 3rd ed., Springer, New York.
(36) Quinti, L., Dayalan Naidu, S., Trager, U., Chen, X., Kegel-Gleason, K., Lleres, D., Connolly, C., Chopra, V., Low, C., Moniot, S., Sapp, E., Tousley, A. R., Vodicka, P., Van Kanegan, M. J., Kaltenbach, L. S., Crawford, L. A., Fuszard, M., Higgins, M., Miller, J. R. C., Farmer, R. E., Potluri, V., Samajdar, S., Meisel, L., Zhang, N., Snyder, A., Stein, R., Hersch, S. M., Ellerby, L. M., Weerapana, E., Schwarzschild, M. A., Steegborn, C., Leavitt, B. R., Degterev, A., Tabrizi, S. J., Lo, D. C., DiFiglia, M., Thompson, L. M., Dinkova-Kostova, A. T., and Kazantsev, A. G. (2017) KEAP1-modifying small molecule reveals muted NRF2 signaling responses in neural stem cells from Huntington's disease patients. *Proc. Natl. Acad. Sci. U. S. A. 114*, E4676−E4685.
(37) Bertrand, H. C., Schaap, M., Baird, L., Georgakopoulos, N. D., Fowkes, A., Thiollier, C., Kachi, H., Dinkova-Kostova, A. T., and Wells, G. (2015) Design, Synthesis, and Evaluation of Triazole Derivatives That Induce Nrf2 Dependent Gene Products and Inhibit the Keap1−Nrf2 Protein-Protein Interaction. *J. Med. Chem. 58*, 7186−7194.

DOI: 10.1021/acs.chemrestox.8b00354
Chem. Res. Toxicol. 2019, 32, 500−512

(38) Vogel, S. S., Thaler, C., and Koushik, S. V. (2006) Fanciful FRET. *Sci. Signaling 2006*, re2.
(39) Chen, X., Zaro, J. L., and Shen, W. C. (2013) Fusion protein linkers: property, design and functionality. *Adv. Drug Delivery Rev. 65*, 1357−1369.
(40) Iizuka, R., Yamagishi-Shirasaki, M., and Funatsu, T. (2011) Kinetic study of de novo chromophore maturation of fluorescent proteins. *Anal. Biochem. 414*, 173−178.
(41) Pedelacq, J. D., Cabantous, S., Tran, T., Terwilliger, T. C., and Waldo, G. S. (2006) Engineering and characterization of a superfolder green fluorescent protein. *Nat. Biotechnol. 24*, 79−88.
(42) Khmelinskii, A., Keller, P. J., Bartosik, A., Meurer, M., Barry, J. D., Mardin, B. R., Kaufmann, A., Trautmann, S., Wachsmuth, M., Pereira, G., Huber, W., Schiebel, E., and Knop, M. (2012) Tandem fluorescent protein timers for in vivo analysis of protein dynamics. *Nat. Biotechnol. 30*, 708−714.
(43) Koushik, S. V., and Vogel, S. S. (2008) Energy migration alters the fluorescence lifetime of Cerulean: implications for fluorescence lifetime imaging Forster resonance energy transfer measurements. *J. Biomed. Opt. 13*, 031204.
(44) Day, R. N. (2014) Measuring protein interactions using Forster resonance energy transfer and fluorescence lifetime imaging microscopy. *Methods 66*, 200−207.
(45) Watai, Y., Kobayashi, A., Nagase, H., Mizukami, M., McEvoy, J., Singer, J. D., Itoh, K., and Yamamoto, M. (2007) Subcellular localization and cytoplasmic complex status of endogenous Keap1. *Genes Cells 12*, 1163−1178.

DOI: 10.1021/acs.chemrestox.8b00354
Chem. Res. Toxicol. 2019, 32, 500−512